Article

Fast Experimental Magnetic Model Identification for Synchronous Reluctance Motor Drives

Vasyl Varvolik [1,*] **, Shuo Wang** [1] **, Dmytro Prystupa** [1] **, Giampaolo Buticchi** [1] **, Sergei Peresada** [2] **, Michael Galea** [3] **and Serhiy Bozhko** [4]

[1] Key Laboratory of More Electric Aircraft Technology of Zhejiang Province, The University of Nottingham Ningbo China, Ningbo 315100, China; Shuo.Wang@nottingham.edu.cn (S.W.); Dmytro.Prystupa@nottingham.edu.cn (D.P.); Giampaolo.Buticchi@nottingham.edu.cn (G.B.)

[2] Department of Electrical Engineering, National Technical University of Ukraine "Igor Sikorsky Kyiv Polytechnic Institute", 03056 Kyiv, Ukraine; sergei.peresada@gmail.com

[3] Department of Industrial Electrical Power Conversion, University of Malta, MSD 2080 Msida, Malta; michael.d.galea@um.edu.mt

[4] PEMC Group, University of Nottingham, Nottingham NG7 2RD, UK; Serhiy.Bozhko@nottingham.ac.uk

* Correspondence: Vasyl.Varvolik@nottingham.edu.cn; Tel.: +86-19883001755

Abstract: The accurate magnetic model is mandatory for high-performance control of high anisotropy synchronous machines. This paper presents a time-efficient and accurate magnetic model identification based on triangle current injection while the machine under the test is driven at a constant speed by a prime mover. The current injection pattern allows scanning the whole range of current, reducing the identification time compared to the standard constant-speed method (CSM) with the same level of accuracy. The ohmic voltage drop and inverter nonlinearities are compensated by using the average voltage of motor and generator modes. The synchronous reluctance machine is used as a case study for validation through the comparison between the experimental results obtained by the proposed method and the CSM against finite element simulation. Moreover, the temperature variation of the machine winding is measured showing no considerable changes during the identification test.

Keywords: magnetic model identification; constant-speed method; flux maps; dead-time

1. Introduction

In recent years, synchronous reluctance (SynRel) motor drives have drawn considerable attention from academia and industry [1]. SynRel drives are widely used in low-cost adjustable-speed applications such as pumps, fans, and home appliances due to manufacturing simplicity, rigid structure, higher efficiency, and torque density compared to induction machines (IM). SynRel exhibits high magnetic nonlinearity due to saturation and cross-saturation phenomena thus a conventional linear magnetic model based on lumped parameters cannot be used and an accurate magnetic model is required to guarantee high-performance control.

The magnetic model represents the relationship between phase currents and flux linkages [2]. Usually, the synchronous reference (*d-q*) frame is used to express flux linkages in a form of two-dimensional look-up tables (LUT) depending on the selected model type either currents or flux linkages are state variables [3]. In order to include the spatial harmonics, the magnetic model is extended with electrical position, however, it results in a higher computational burden because of three-dimensional LUTs and mainly can be used in high fidelity simulation required for a hardware-in-loop (HIL) [4].

Research publications present several methods regarding accurate magnetic model identification (MMI) and can be classified into online and offline techniques [5]. Most of the online methods fall into current, voltage, and high-frequency signal injection (an overview is beyond the scope of this paper and is presented in [6]). They are executed in parallel with

the main control algorithm estimating, for example, incremental inductances as presented in [7] which increases the computational complexity of the control algorithm. Offline techniques represent a broader spectrum of methods which can be divided into analytical and experimental methods [2,8]. The former group requires detailed information about machine design such as stator and rotor geometry, materials, and winding configuration in order to run the finite-element analysis (FEA) [9] or set up the analytical model based on a simplified magnetic circuit [10]. However, the design data are not always available and the accuracy is not guaranteed due to manufacturing imperfections.

The experimental methods include AC/DC signal injection, constant-speed identification, dynamic identification, locked rotor identification, and self-commissioning.

The magnetic model can be derived from the frequency response to AC signal injection and time response to DC signal injection [11]. The most common is single-phase configuration when the one phase is supplied with AC voltage injecting current up to the rated value to estimate the flux linkage curves, however, it requires additional hardware, such as an AC voltage source and measuring equipment.

The constant-speed identification method (CSM) proposed in [2] is the state-of-the-art of the MMI in terms of flux linkages estimation accuracy. During the identification, the machine under the test is current-controlled, and different d- and q-axis reference currents are imposed according to the area of evaluation while it is driven at a constant speed by a prime mover. Flux linkages are estimated using (d-q) voltage terms at steady-state. Spatial harmonics and inverter dead-time are eliminated by averaging the measurements over one mechanical period, similarly, resistance voltage drops and inverter nonlinearities are taken into account by the average between motoring and generating modes. It requires a regenerative DC power supply or braking chopper for both drives if the DC link is not shared. The main limitation for the industrial end-of-line implementation is the considerable identification time.

Dynamic identification methods do not require a prime mover and can be used if the shaft is free to rotate. The machine is accelerated and decelerated by imposing a predefined pattern of d- and q-axis reference currents by the current vector controller [12]. The flux linkage average of the acceleration/deceleration at the same speed reduces the effects of inverter nonlinearities as well as resistance voltage drops. Similarly, the motor-generator dynamic method is proposed in [13,14]. It makes use of estimated flux linkages in motor/generator modes at the same speed. The acceleration is defined by the total moment of inertia thus the maximum speed should be controlled. The main limitations are related to low torque (especially no-torque) and high torque areas. In the former case, there is no acceleration/deceleration. In the latter case, the opposite situation can happen when the acceleration is too fast for sufficient data acquisition.

Standstill identification includes locked rotor identification and self-commissioning techniques. In the case of a rotor locking the d-axis current is kept constant while voltage pulses are applied along with q-axis as proposed in [15]. The flux maps are obtained by voltage integration and verified against FEA results. Self-commissioning is in great demand on the market because it is done by the electric drive without any additional hardware and unwanted rotor movement [16]. Therefore several methods have been proposed in [8,17–19] mainly based on the bipolar voltage injection of high amplitude to minimize the influence of stator resistance inaccuracy and inverter nonlinearities. The injected voltage is integrated to derive the flux linkages in the same manner as the locked rotor method showing sufficient accuracy. However, common flaws of standstill methods are the flux estimation drift due to the voltage integration and the identification accuracy deterioration caused by not properly compensated inverter nonlinearities [20].

This paper proposes a time-efficient magnetic model identification technique for high anisotropy synchronous machines based on the constant-speed method [2]. Employing the symmetrical triangle current injection pattern allows to sweep the whole range of currents instead of one operation point per cycle without losing accuracy, therefore, the identification test time is dramatically reduced compared to the CSM. The voltage disturbances

caused by spatial harmonics and inverter nonlinearities are minimized by applying the moving window average. Additionally, the proposed current injection sequence excludes the current derivative influence and the torque discontinuity. The winding operating temperature measurements during the identification process show its negligible effect on the stator resistance due to the reduced test time. The accuracy of the estimated flux linkage maps is verified by comparing the proposed method and the conventional CSM against FEA simulation results.

2. Proposed Triangle Current Injection Constant-Speed Method

2.1. Principle of Flux Linkages Identification

The voltage balance equations for the SynRel in the synchronously rotating reference (*d-q*) frame considering a nonlinear current–flux relationship are given as [21]

$$\begin{cases} u_d = R_s i_d + \dfrac{d\psi_d(i_d, i_q)}{dt} - \omega_e \psi_q(i_d, i_q) \\ u_q = R_s i_q + \dfrac{d\psi_q(i_d, i_q)}{dt} + \omega_e \psi_d(i_d, i_q) \end{cases} \tag{1}$$

where u_d and u_q are the stator voltage components, i_d and i_q are the stator current components, ψ_d and ψ_q are the stator flux components of (*d-q*) axes, ω_e is the electrical speed, and R_s is the stator resistance.

The time derivatives of flux terms are defined as functions of current derivatives

$$\begin{cases} \dfrac{d\psi_d(i_d, i_q)}{dt} = \dfrac{\partial \psi_d}{\partial i_d} \dfrac{di_d}{dt} + \dfrac{\partial \psi_d}{\partial i_q} \dfrac{di_q}{dt} = l_{dd} \dfrac{di_d}{dt} + l_{dq} \dfrac{di_q}{dt} \\ \dfrac{d\psi_q(i_d, i_q)}{dt} = \dfrac{\partial \psi_q}{\partial i_d} \dfrac{di_d}{dt} + \dfrac{\partial \psi_q}{\partial i_q} \dfrac{di_q}{dt} = l_{qd} \dfrac{di_d}{dt} + l_{qq} \dfrac{di_q}{dt} \end{cases} \tag{2}$$

where l_{dd} is the *d*-axis incremental (differential) inductance, l_{qq} the *q*-axis incremental inductance, and $l_{dq} = l_{qd}$ are the mutual incremental cross-saturation inductances.

The constant-speed [2] and dynamic identification [12–14] methods are based on the (i_d, i_q) current steady-state assuming the constant flux linkage and neglecting the flux derivative term from the voltage (Equation (1)). The area of identification is organized in the rectangular current mesh and defines the (i_d^*, i_q^*) reference currents which are sequentially imposed by proportional-integral (PI) current controllers. The current steady-state for every set point has to be reached as well as the idle time has to be added to eliminate a stator resistance variation. It results in a significant identification time thus the triangle current injection constant-speed method (TCICSM) is presented to reduce the estimation time keeping the same level of accuracy. Figure 1 shows the proposed identification test sequence.
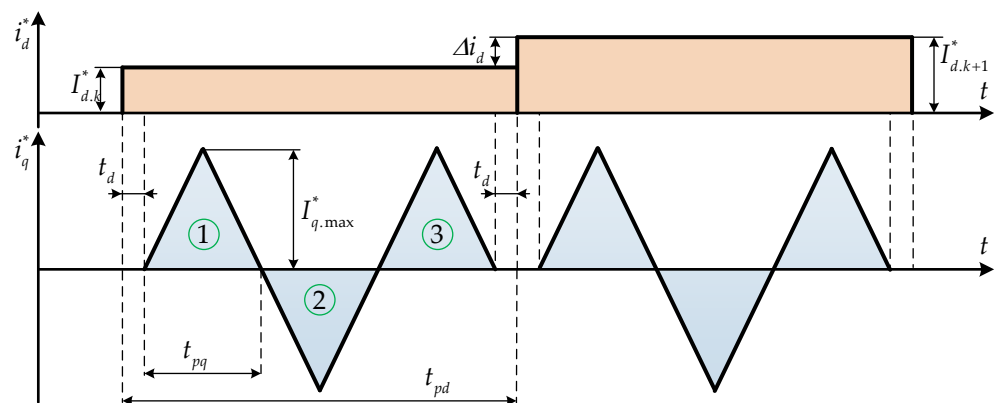

Figure 1. Proposed identification test sequence.

As shown in Figure 1, the *d*-axis reference current is changed gradually by predefined step Δi_d, meanwhile, the *q*-axis current is made up of a symmetrical triangle waveform with a peak amplitude of $\pm I_{q.max}$. The *q*-axis is chosen for triangle waveform injection because of the saliency ratio of SynRel ($l_{dd} > l_{qq}$) to minimize the derivative term in (2). Similar to the CSM, the test includes two motoring and one generating modes in order to compensate for ohmic voltage drop and inverter nonlinearities, however, instead of one operation point the whole range of *q*-axis currents are explored, allowing to neglect idle time due to reduced test time. It is important to start i_q current injection only after electrical transient of the i_d current when it has reached the steady-state for that reason the time delay t_d is inserted.

According to proposed identification method, the voltage equations can be rewritten replacing the flux time derivatives in (1) by incremental inductances and assuming that *d*-axis current has reached its set point thus its derivative can be approximated to zero as

$$\begin{cases} u_d = R_s i_d + l_{dd}\dfrac{di_d}{dt} + l_{dq}\dfrac{di_q}{dt} - \omega_e\psi_q(i_d,i_q) = R_s i_d + l_{dq}\dfrac{di_q}{dt} - \omega_e\psi_q(i_d,i_q) \\ u_q = R_s i_q + l_{qd}\dfrac{di_d}{dt} + l_{qq}\dfrac{di_q}{dt} + \omega_e\psi_d(i_d,i_q) = R_s i_q + l_{qq}\dfrac{di_q}{dt} + \omega_e\psi_d(i_d,i_q) \end{cases} \quad (3)$$

The *q*-axis current derivative can be taken into account by using a symmetrical triangle reference. When the current is increasing or decreasing the derivative is positive or negative respectively, therefore, the voltage can be averaged excluding the derivative terms from the voltage Equation (3) as

$$\begin{cases} u_{d.avg} = \dfrac{1}{2}(u_{d.up} + u_{d.down}) = \dfrac{1}{2}\left(2\cdot R_s i_d + l_{dq}\dfrac{di_{q.\nearrow}}{dt} - l_{dq}\dfrac{di_{q.\searrow}}{dt} - 2\omega_e\psi_q(i_d,i_q)\right) \\ u_{q.avg} = \dfrac{1}{2}(u_{q.up} + u_{q.down}) = \dfrac{1}{2}\left(2\cdot R_s i_q + l_{qq}\dfrac{di_{q.\nearrow}}{dt} - l_{qq}\dfrac{di_{q.\searrow}}{dt} + 2\omega_e\psi_d(i_d,i_q)\right) \end{cases} \quad (4)$$

From Equation (4), the voltage equations for flux estimation are obtained

$$\begin{cases} u_{d.avg} = R_s i_d - \omega_e\psi_q(i_d,i_q) \\ u_{q.avg} = R_s i_q + \omega_e\psi_d(i_d,i_q) \end{cases} \quad (5)$$

The average voltage $u_{q.avg}$ calculation for one positive triangle for $i_d = 40$ A, $i_q = 0..40$ A is shown in Figure 2. The voltage values are averaged between symmetrical samples as highlighted by two blue dots t_1 and t_2 and the resulting voltage curve.
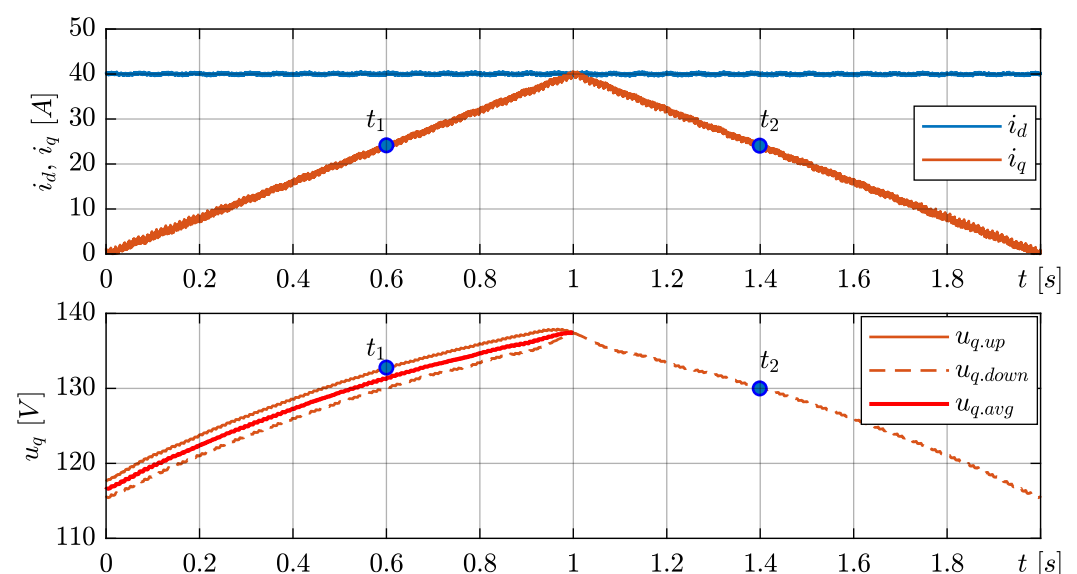

Figure 2. Voltage averaging for current derivative elimination.

It should be noticed that the *d*-axis pulse width, the *q*-axis ramp time of the triangle, and the time delay (according to Figure 1) are chosen to ensure proper current tracking. The flux linkages can be estimated using (5) as

$$\begin{cases} \psi_d(i_d, i_q) = \dfrac{u_{q.avg} - R_s i_q}{\omega_e} \\ \psi_q(i_d, i_q) = -\dfrac{u_{d.avg} - R_s i_d}{\omega_e} \end{cases} \tag{6}$$

However, using (6) provides the accurate flux estimation only if the stator resistance is known and the inverter nonlinearity effects caused by the dead-time and on-state voltage errors are properly compensated, therefore, the proposed technique is based on averaging of motoring and generating modes [2,13,22]. It makes the identification method inherently robust to voltage errors. The flux linkage is estimated as

$$\begin{cases} \psi_d(i_d, i_q) = \dfrac{1}{2} \cdot \left(\dfrac{u_{q.avg.\triangle.1} + u_{q.avg.\triangle.3.}}{2} + u_{q.avg.\triangle.2} \right) \cdot \dfrac{1}{\omega_e} \\ \psi_q(i_d, i_q) = -\dfrac{1}{2} \cdot \left(\dfrac{u_{d.avg.\triangle.1} + u_{d.avg.\triangle.3.}}{2} - u_{d.avg.\triangle.2} \right) \cdot \dfrac{1}{\omega_e} \end{cases} \tag{7}$$

where subscripts $\triangle.1$ and $\triangle.3$ correspond to motoring mode (first and third triangle) and $\triangle.2$ corresponds to generating mode (second triangle) according to Figure 1.

The inverter reference voltage is used for flux estimation due to the difficulties of pulse-width modulation (PWM) measurement and additional cost. However, the reference voltage has disturbances caused by spatial harmonics and inverter dead-time and cannot be directly used for flux estimation. In the CSM these effects are eliminated by voltage averaging over one mechanical period but in the proposed method it cannot be applied due to a specific *q*-axis current pattern. Therefore, a moving window average is employed in order to minimize voltage disturbances. The window slides along the recorded data samples, computing the centered average for the element in the current position plus the surrounding neighbors inside of the window. The average for voltage vector u_{dq} is defined as

$$\overline{u}_{dq}(i) = \dfrac{1}{N_s} \sum_{i=1}^{N_s} u_{dq}(i) \tag{8}$$

where $\overline{u}_{dq}$ is averaged voltage components, N_s is averaging window length.

The window length is specified as the number of samples per one electrical period as follows

$$N_s = \dfrac{60}{n_m p_n T_s} \tag{9}$$

where n_m is mechanical speed, p_n is pole pair number, and T_s is sampling time.

In Figure 3, an example of moving average for u_{dq} voltages is shown.
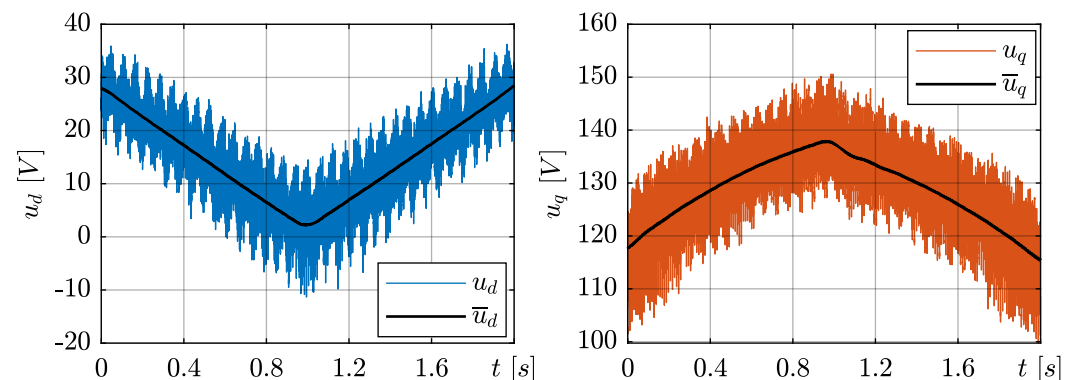

Figure 3. Voltage moving average for $i_d = 40$ A, $i_q = 0..40$ A.

It is recommended to apply the moving average to the (i_d, i_q) currents to reduce the measurement noise and periodic disturbances, especially when the dead-time is not compensated.

2.2. Finite Element Model of SynRel

The FE analysis of the SynRel is used as a benchmark for the evaluation of the magnetic model identification accuracy. The FE model is set up based on the design data reported in Table 1 [23], the cross-section and an example of flux density map are shown in Figure 4.

Table 1. Main data of the considered SynRel prototype.

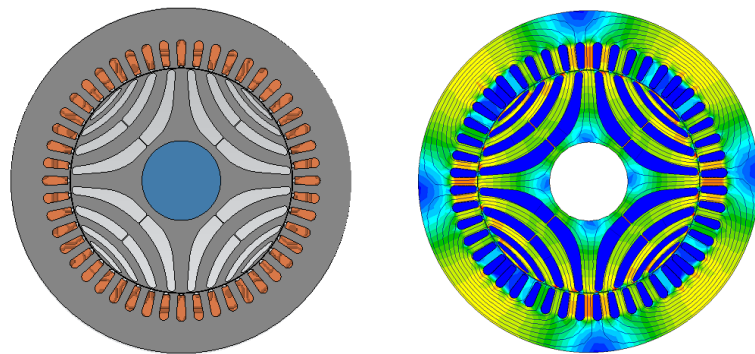| Parameter	Value	Parameter	Value
DC link voltage (V)	540	Stator diameter (mm)	260
Rated current (Apk)	44.2	Airgap thickness (mm)	0.5
Rated power (kW)	15	Rotor diameter (mm)	169
Rated torque (Nm)	95	Stack length (mm)	205

Figure 4. Cross-section of the SynRel FEA model (**left**) and an example of flux density map (**right**).

A series of FEA simulations have been carried out according to the predefined (i_d, i_q) currents plane as 40×40 A. The computed flux maps for *d*- and *q*-axes are presented in Figure 5.
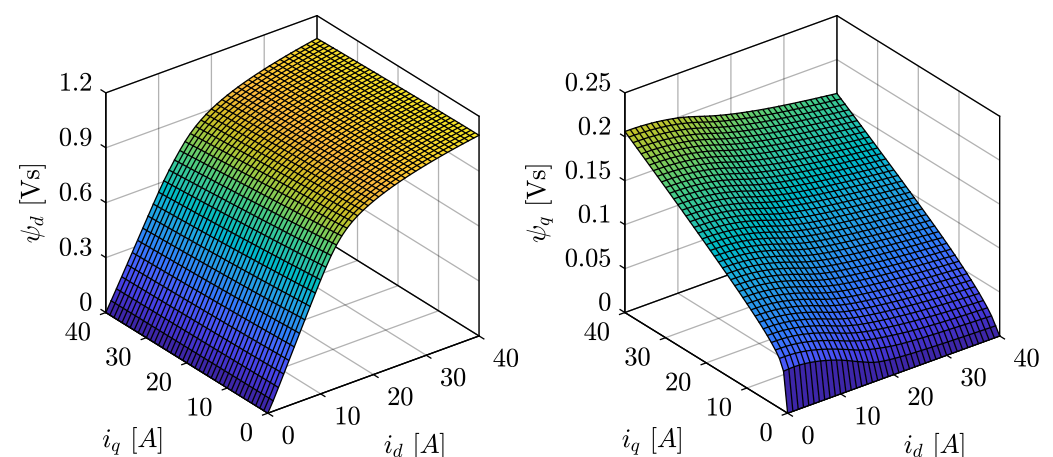

Figure 5. Flux maps *d*-axis flux linkage (**left**) and *q*-axis flux linkage (**right**).

The electromagnetic torque map of the machine can be retrieved by FEA simultaneously with the flux maps or calculated during the data post-processing based on the flux linkage as

$$T_{em} = \frac{3}{2} p_n (\psi_d(i_d, i_q) i_q - \psi_q(i_d, i_q) i_d) \tag{10}$$

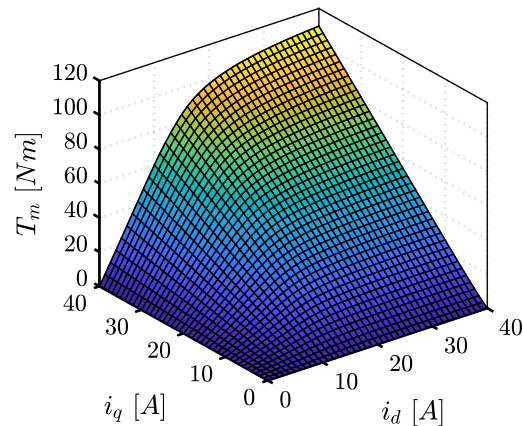The computed torque map by means of FEA is shown in Figure 6.

Figure 6. Electromagnetic torque map.

3. Hardware Implementation

The experimental setup for the proposed TCICSM and the CSM requires a machine under the test to be coupled with a speed-controlled prime mover as shown in Figure 7.
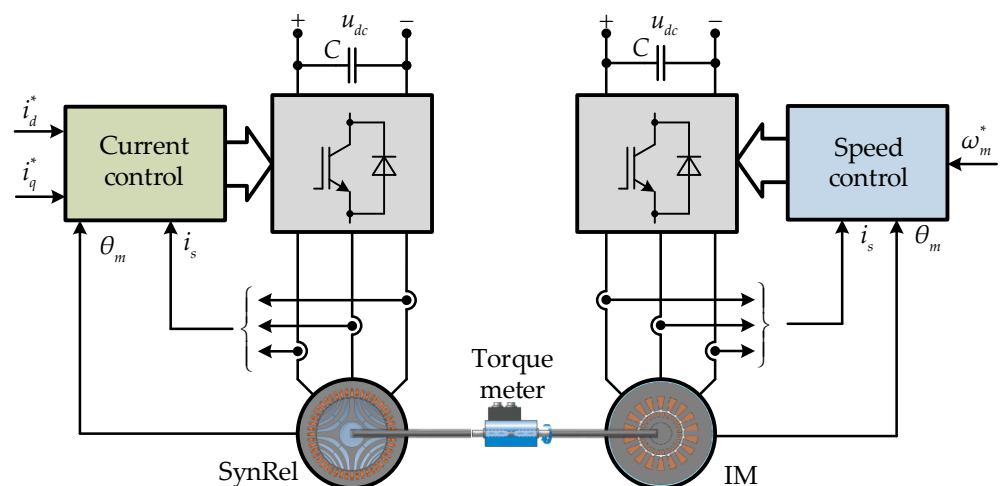

Figure 7. Block scheme of magnetic model identification setup.

As was mentioned before, the tested machine is current-controlled and requires position feedback (resolver or encoder). The initial rotor position alignment is done by the voltage or current injection along the α-axis, the rotor starts rotation until it reaches a stable position aligned with the corresponding axis, and then the position sensor offset is set to zero.

It is highly important to emphasize that the identification scheme must be regenerative for both the machine under test and the speed-controlled prime mover or connected to a common DC link.

The presence of a torque sensor allows verification of estimation results by comparing the measured torque map with calculated based on the identified flux maps, however, it is not compulsory.

The experimental test bench is represented in Figure 8. The machine under the test (SynRel 15 kW prototype) is on the left-hand side. The torque transducer (Kistler 4503A200WA2B100) is mounted between the two shafts. The rotor position is measured by means of a resolver (Tamagawa TS2225N922E102) installed on the non-drive end of the SynRel motor. The industrial drive with an induction machine (AMP Series 132-40 kW/rated torque is 212 Nm) is used as a prime mover is on the right-hand side. The

torque redundancy of prime mover allows the overload current area evaluation of the SynRel. Both drives are connected to a regenerative power source. The TCICSM and the CSM are implemented using a dSPACE MicroLabBox platform which controls a three-phase IGBT-based inverter via an interface board. The sampling frequency and dead-time were set to 10 kHz with dead-time 4 µs, respectively.
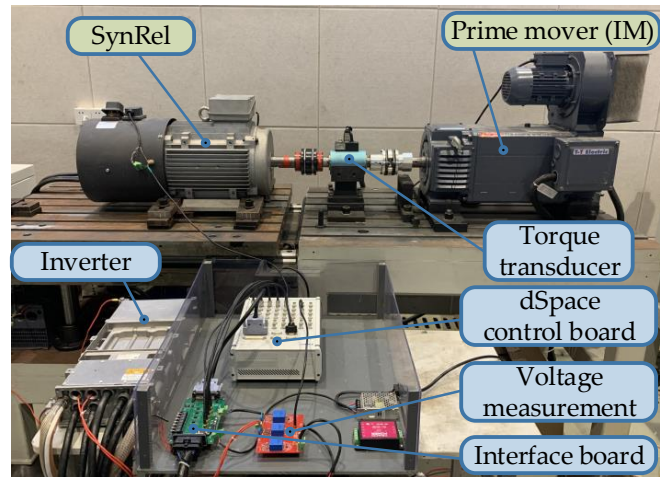

Figure 8. Test bench for magnetic model identification [23].

4. Experimental Results

The magnetic model identification has been done by means of the CSM and the proposed TCICSM. Before performing the tests the PI current controllers were roughly tuned without prior knowledge of the magnetic model and fixed gains were used for all experiments. The reference speed of the prime mover was set to 500 rpm (one-third of the base speed) in order to minimize the influence of iron losses and provide a good signal-to-noise ratio for the voltage measurement. The DC link voltage was set to 540 V.

4.1. Constant-Speed Method Identification

The active and idle time durations for the CSM were selected according to the recommendations in [2]. The three current pulses duration was set at 1.5 s to exclude any transients and guarantee the average calculation of all measurements over two mechanical periods, the idle time was set equal to active time, not doubled, because the tested SynRel is equipped with an embedded cooling fan. The area of identification is 40×40 A.

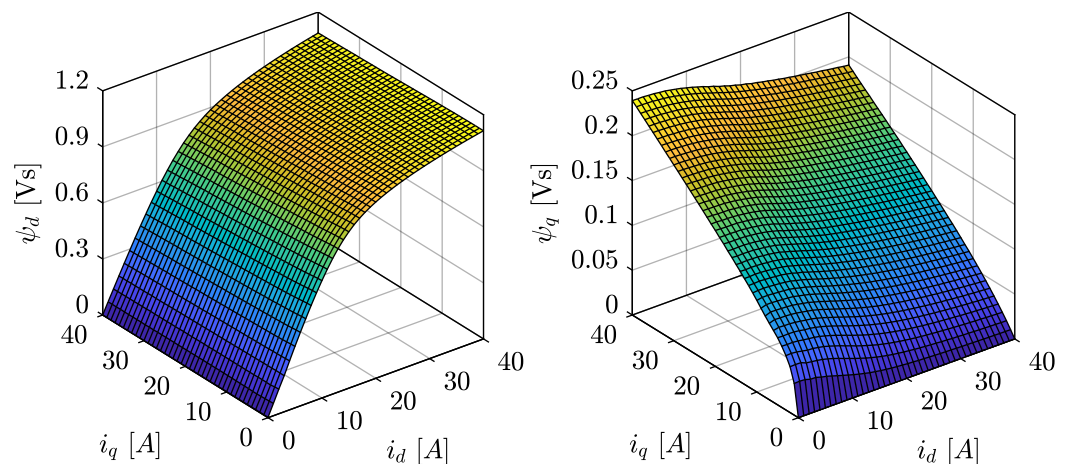The identified flux linkage maps are illustrated in Figure 9.

Figure 9. Identified *d*-axis flux linkage (**left**) and *q*-axis flux linkage (**right**) maps by CSM.

The experimentally obtained results are compared with those derived by means of FE simulation considered as a benchmark. The mismatch between the flux linkages obtained by the benchmark method and the conventional constant-speed/TCICSM identification results are defined as estimation differences. The normalized difference is defined as [5]

$$\Delta \psi_{dq} = \frac{|\psi_{dq.FEA} - \hat{\psi}_{dq}|}{max(\hat{\psi}_{dq})} \cdot 100 [\%] \tag{11}$$

where $\psi_{dq.FEA}-$ flux values obtained by FE simulation, $\hat{\psi}_{dq}-$ estimated flux linkages, and $max(\hat{\psi}_{dq})$ is the maximum value of flux linkage along the corresponding axis.

The flux estimation differences between the benchmark method and the CSM are presented in Figure 10, the rated point is highlighted by the red dot.
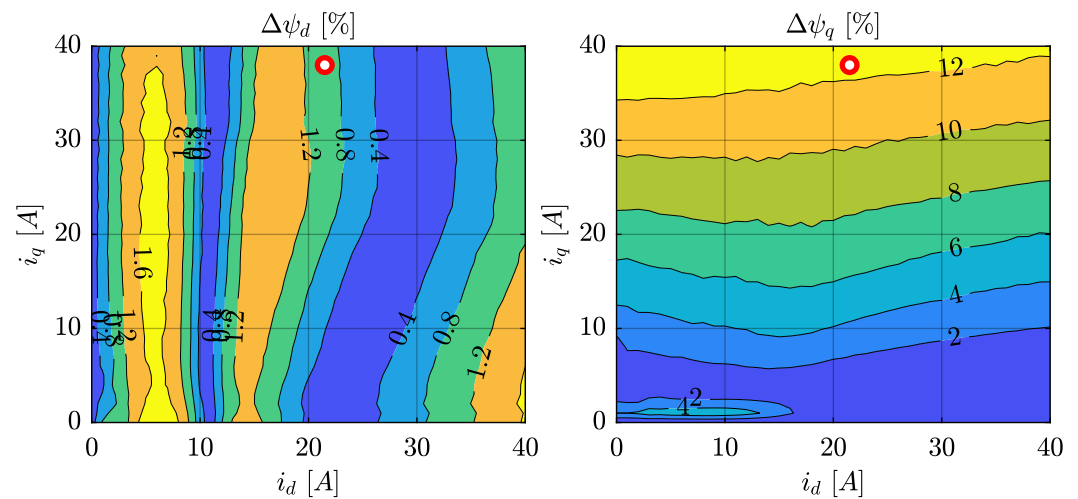

Figure 10. Flux linkage estimation difference *d*-axis (**left**) and *q*-axis (**right**) for the CSM.

As can be seen, the maximum normalized flux differences are 1.9 % and 13.8% for the *d*- and *q*-axes, respectively. Such mismatch, especially in the *q*-axis, can be caused by the manufacturing process tolerance. As an example, if the rotor has been manufactured with a tolerance of 0.05 mm and all the iron bridges are at the upper limit thus the total bridge per barrier goes from 2 mm (two tangential bridges of 0.75 mm + one radial of bridge 0.5 mm) to 2.15 mm, resulting in a reduction of the *q*-axis flux.

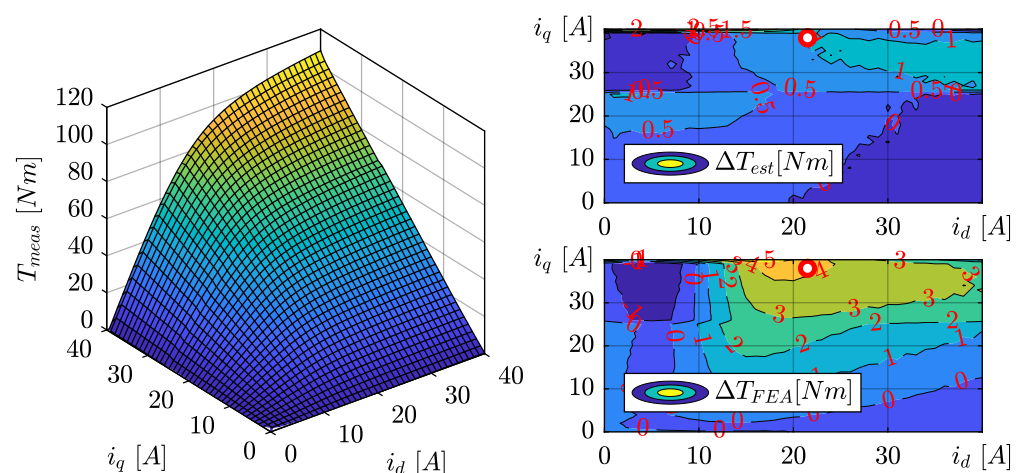Figure 11 shows the measured torque map on the left and difference contours on the right.

Figure 11. Measured torque map (**left**) and torque difference contours (**right**) for the CSM.

The torque difference contours are used for additional validation of the identified magnetic model and calculated as

$$\Delta T_{est/FEA} = T_{est/FEA} - T_{meas} \tag{12}$$

where T_{est} is a torque map derived by means of estimated flux values applying (1), T_{FEA} is a torque map retrieved by FEA simulations, and T_{meas} is a measured torque map during the identification test.

The maximum mismatch for ΔT_{est} is 3.19 Nm and ΔT_{FEA} for is 5.8 Nm which correspond to relative differences concerning the maximum measured torque of 2.95% and 5.37%, respectively. Taking into account measurement inaccuracy and friction the results show good agreement.

4.2. Proposed Triangle Current Injection Constant-Speed Method

The proposed identification technique has been tested with the following time settings—the d-axis reference current pulse width t_{pd} = 6.2 s, the q-axis reference current ramp time t_{pq} = 2 s, and delay t_d = 0.1 s according to Figure 1. The identification area is defined as 40 × 40 A, with a step of 1 A along the d-axis. Considering a time step set as 6.2 s for one reference cycle, the total time required for the flux mapping was about 4 min.

The d- and q-axis currents and reference voltage waveforms during the magnetic model identification process are shown in Figure 12.
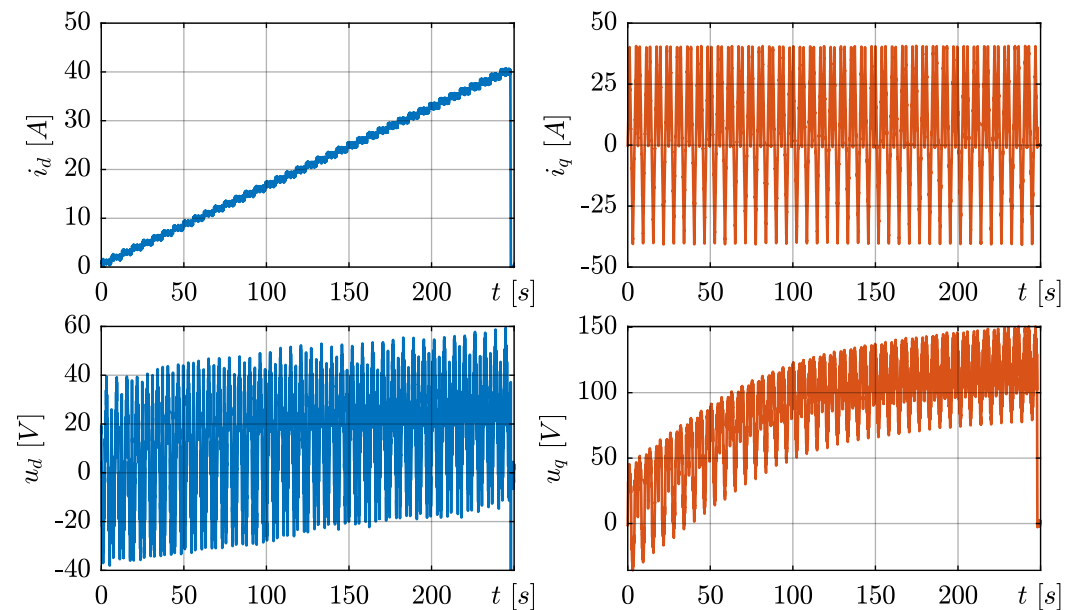

Figure 12. Current and reference voltage waveforms during the complete identification process.

The zoomed view of one identification cycle of (d-q) current, reference voltages, and torque waveforms are illustrated in Figure 13. In order to calculate flux linkage values, the measurements need to be post-processed according to the proposed identification technique. Firstly, the moving window average is applied to the reference voltages u_{dq} and the moving average voltage waveforms $\overline{u}_{dq}$ are obtained, the window size is set to N_s = 600 samples which correspond to one electrical period at the speed of 500 rpm. Then the moving average voltage waveforms are divided into six intervals (blue and yellow shaded) according to the q-axis current derivative sign and motor operating mode. Finally, the voltage average is calculated between $\overline{u}_{dq}$ voltages corresponding to symmetrical current points for each triangle to eliminate the influence of the q-axis current derivative and (7) is applied to estimate the flux linkages.
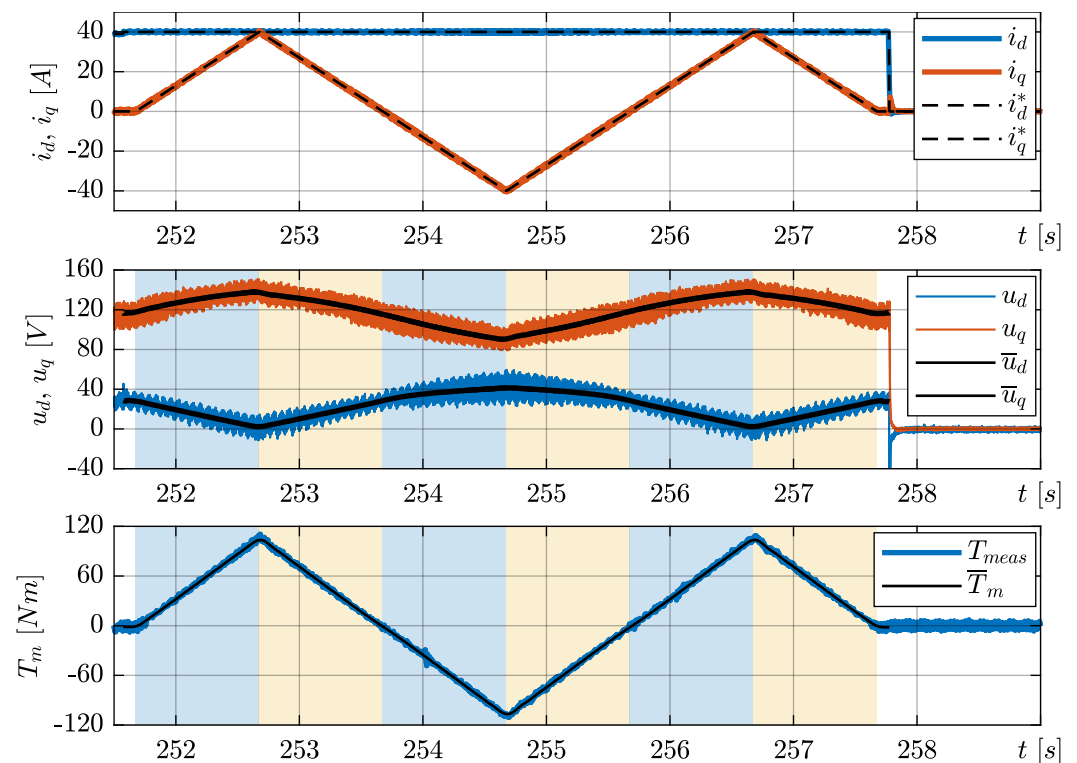
Figure 13. Identification sequence for one current combination $i_d = 40$ A and $i_q = -40..40$ A at $n_m = 500$ rpm.

It can be seen that the torque dynamic is properly controlled during the identification. This avoids the torque discontinuity which normally occurs during the CSM test while switching between the motoring and generating modes. It allows minimizing the effects of vibrations and shocks on the mechanical part of the machine under the test.

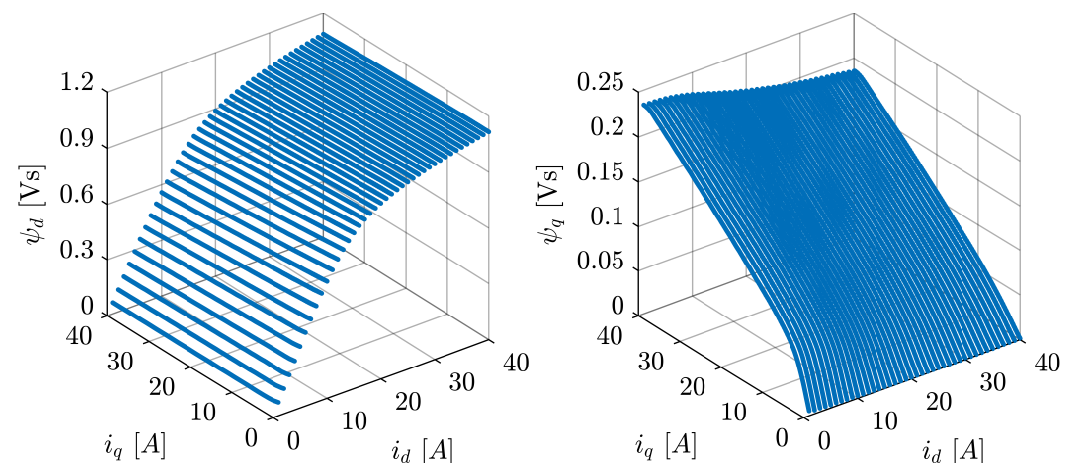The calculated flux linkage samples are plotted in 3-D space as shown in Figure 14.

Figure 14. Estimated flux linkage samples *d*-axis (**left**) and *q*-axis (**right**).

As can be noted, the estimated flux linkage samples are regularly spaced with the predefined step of 1 A along *d*-axis and can be regarded as continuous along *q*-axis. It brings additional benefits for high-performance control of SynRel such as model predictive control [24] because the incremental inductances l_{dq} , l_{qq} can be calculated with adjustable current step and higher accuracy.

The flux estimation differences between the benchmark method and proposed TCICSM are reported in Figure 15.
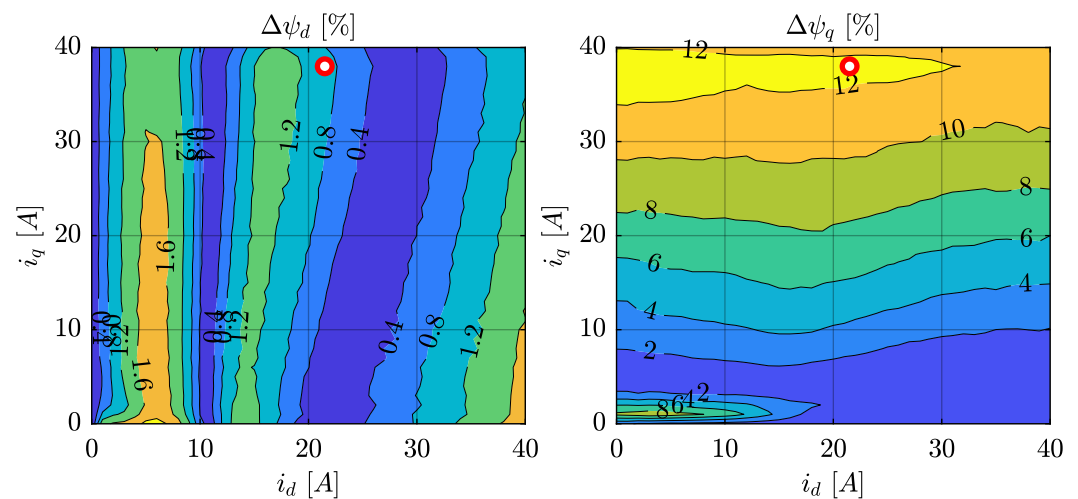
Figure 15. Flux linkage estimation difference *d*-axis (**left**) and *q*-axis (**right**) for the TCICSM.

From the comparison with Figure 10, it can be concluded that the normalized flux difference maps have a very good agreement. In case of the TCICSM, the maximum normalized flux differences are 2.18 % and 13.3% for the *d*- and *q*-axes, respectively.

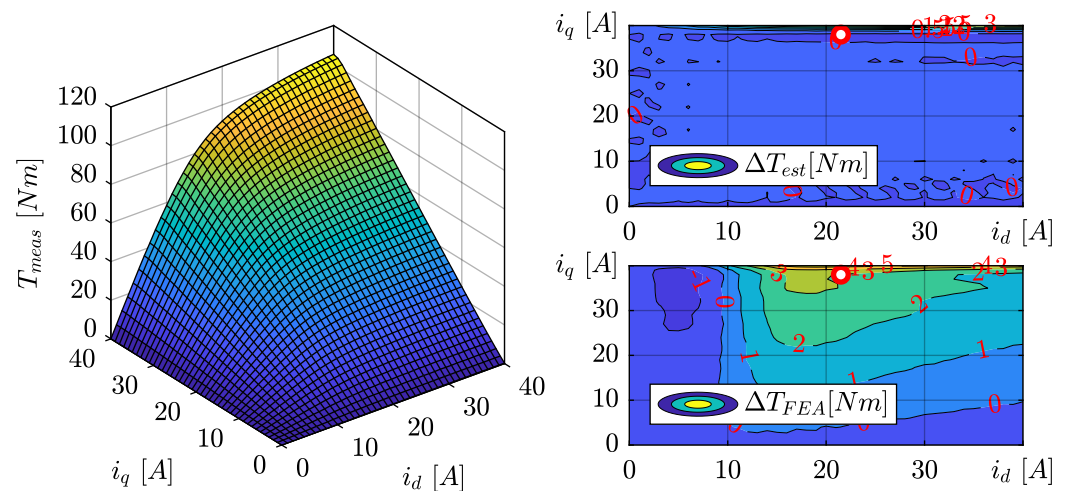The measured torque map during identification and difference contours are presented in Figure 16.

Figure 16. Measured torque map (**left**) and torque difference contours (**right**) for the TCICSM.

The measured torque map comparison with the estimated torque by means of identified flux linkages shows the maximum difference for ΔT_{est} is 3.264 Nm corresponding to the relative difference of 3.02 % with respect to the maximum measured torque. The comparison of the measured torque map with FE results shows a bigger mismatch with the maximum difference for ΔT_{FEA} is 5.54 Nm corresponding to the relative difference of 5.13%.

Overall, the CSM and the proposed TCICSM results are very similar compared to the benchmark. The summary of the results described is reported in Table 2.

Table 2. Comparison of considered methods (maximum difference values).

Parameter	$\Delta\psi_d$, %	$\Delta\psi_q$, %	ΔT_{est}, Nm	ΔT_{FEA}, Nm	t_{ident}, min
Conventional CSM	1.9	13.8	3.19	5.8	83
Proposed TCICSM	2.2	13.3	3.26	5.5	4

The comparison of the CSM and the TCICSM is done by calculation of normalized difference similarly to (12), as presented in Figure 17.
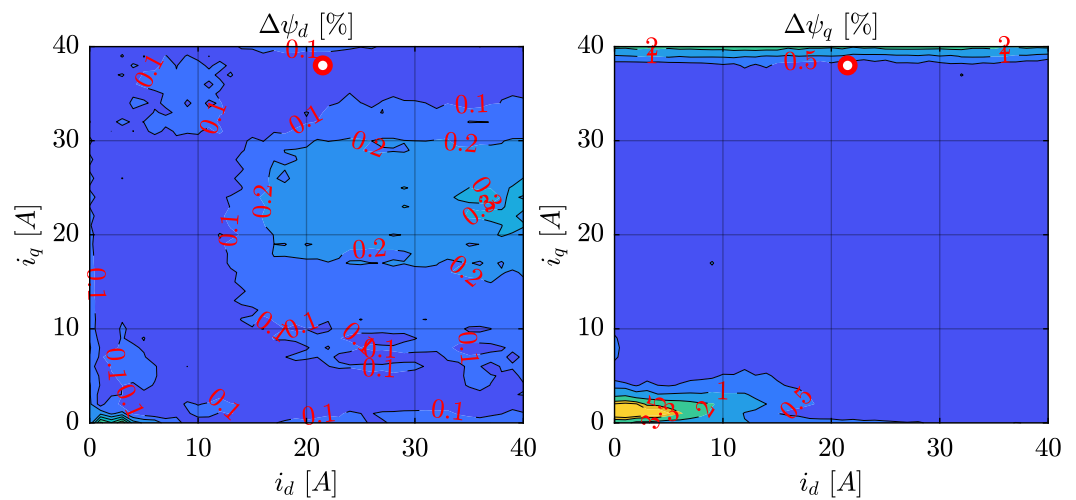

Figure 17. Flux linkage estimation difference between the CSM and proposed method for *d*-axis (**left**) and *q*-axis (**right**).

It can be concluded that there is a good agreement between the CSM and the TCICSM across the identification area (the maximum normalized flux differences are 0.3% and 3.5% for the *d*- and *q*-axes, respectively). The proposed technique allows reducing the identification time without losing accuracy compared to the CSM.

As an application example, the considered magnetic models have been used to compute three MTPA (maximum torque per ampere) control laws for the motor under the test as shown in Figure 18. The green line represents the MTPA trajectory calculated based on FEA results. The red line shows the calculated MTPA trajectory using the constant-speed method and the dashed blue line corresponds to the MTPA trajectory derived by means of the proposed method. It can be seen that trajectories corresponding to the CSM and the TCICSM overlap each other, meanwhile, the FE-based trajectory tends to deviate at high current regions.
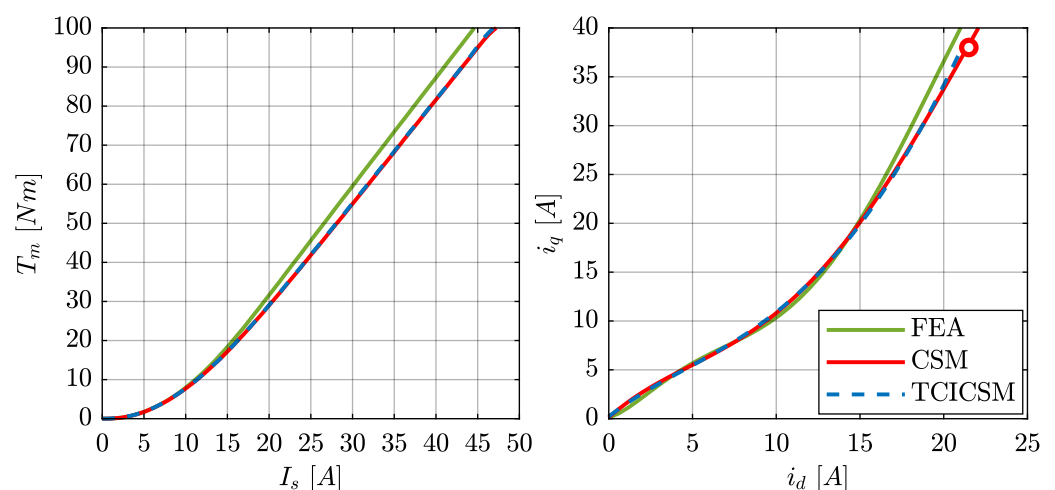

Figure 18. Comparison of MTPA characteristics: maximum torque versus phase current (**left**), control trajectories (**right**).

In order to monitor the operating temperature during the proposed identification test, the temperature sensor was embedded into the machine winding. Figure 19 shows the winding temperature measurements with and without a cooling fan.
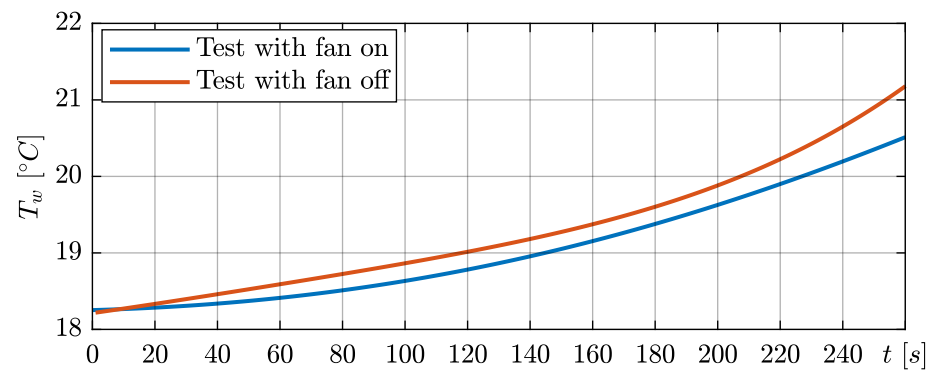
Figure 19. The winding temperature during proposed identification test.

As can be observed, the temperature rise ($\Delta T_{fan.On} \approx 2.26$ °C, $\Delta T_{fan.Off} \approx 3$ °C) of the machine winding throughout the identification test is negligible due to the short identification time. The approximation for the resistance change in respect to the initial value can be calculated as [25]

$$\Delta R_s = \frac{\alpha_{Cu}\Delta T}{R_{s.20°C}} \cdot 100[\%] \approx 5 - 6.5[\%] \tag{13}$$

where $\alpha_{Cu} = 3.81 \cdot 10^{-3}$ K^{-1} is the temperature coefficient for the resistivity of the copper winding, $R_{s.20°C} = 0.173$ Ohm—the measured resistance at room temperature.

5. Conclusions

This paper presents the fast magnetic model identification technique for synchronous reluctance motors based on the constant-speed method. The identification time is dramatically reduced by introducing a new current injection pattern with the same level of accuracy compared to the conventional CSM. The torque discontinuity is not involved, since the triangle current reference exhibits a smoother response than a step reference.

During the data post-processing, the influence of the current derivative is eliminated by making use of the symmetrical current injection pattern. The spatial harmonics and inverter dead-time effects are minimized by applying the moving window average.

The experimental results were evaluated by comparison with FEA simulation regarded as a benchmark method. The CSM and the TCICSM show the same level of accuracy compared to the benchmark, therefore confirming the validity of the proposed method. The total time for conducting this test can be reduced from 83 min to just 4 min. The operating temperature is monitored during the proposed identification test and shows a negligible increase without influence on the test results.

The identified magnetic model can be used to derive the MTPA control trajectory. The comparison of MTPA characteristics shows the importance of experimental flux linkage identification for high-performance control due to the uncertainties during the manufacturing process resulting in inevitable errors of FEA simulation results.

Author Contributions: Conceptualization, V.V., S.W., and G.B.; validation, V.V., S.W., G.B., and D.P.; writing—original draft preparation, V.V.; writing—review and editing, S.W., G.B., D.P., S.P., M.G., and S.B.; supervision, S.W., G.B., D.P., S.P., M.G., and S.B. All authors have read and agreed to the published version of the manuscript.

Institutional Review Board Statement: Not applicable

Conflicts of Interest: The authors declare no conflict of interest.

References

1. Pellegrino, G.; Jahn, T.M.; Bianchi, N.; Soong, W.L.; Cupertino, F. *The Rediscovery of Synchronous Reluctance and Ferrite Permanent Magnet Motors Tutorial Course Notes*; Springer: Berlin/Heidelberg, Germany, 2016.
2. Armando, E.; Bojoi, R.I.; Guglielmi, P.; Pellegrino, G.; Pastorelli, M. Experimental Identification of the Magnetic Model of Synchronous Machines. *IEEE Trans. Ind. Appl.* **2013**, *49*, 2116–2125. [CrossRef]
3. Drobnič, K.; Gašparin, L.; Fišer, R. Fast and Accurate Model of Interior Permanent-Magnet Machine for Dynamic Characterization. *Energies* **2019**, *12*, 783. [CrossRef]
4. Lee, J.; Kwon, Y.C.; Sul, S.K. Identification of IPMSM Flux-Linkage Map for High-Accuracy Simulation of IPMSM Drives. *IEEE Trans. Power Electron.* **2021**, *36*, 14257–14266. [CrossRef]
5. Ortombina, L.; Pasqualotto, D.; Tinazzi, F.; Zigliotto, M. Magnetic Model Identification of Synchronous Motors Considering Speed and Load Transients. *IEEE Trans. Ind. Appl.* **2020**, *56*, 4945–4954. [CrossRef]
6. Zhu, Z.Q.; Liang, D.; Liu, K. Online Parameter Estimation for Permanent Magnet Synchronous Machines: An Overview. *IEEE Access* **2021**, *9*, 59059–59084. [CrossRef]
7. Berto, M.; Alberti, L.; Martin, F.; Hinkkanen, M. Online Incremental Inductance Identification for SynRel Motors. In Proceedings of the IECON 2021—47th Annual Conference of the IEEE Industrial Electronics Society, Toronto, ON, Canada, 13–16 October 2021; pp. 1–6. [CrossRef]
8. Odhano, S.A.; Pescetto, P.; Awan, H.A.A.; Hinkkanen, M.; Pellegrino, G.; Bojoi, R. Parameter Identification and Self-Commissioning in AC Motor Drives: A Technology Status Review. *IEEE Trans. Power Electron.* **2019**, *34*, 3603–3614. [CrossRef]
9. Bianchi, N.; Bolognani, S. Magnetic models of saturated interior permanent magnet motors based on finite element analysis. In Proceedings of the Conference Record of 1998 IEEE Industry Applications Conference. Thirty-Third IAS Annual Meeting (Cat. No.98CH36242), St. Louis, MO, USA, 12–15 October 1998; Volume 1, pp. 27–34. [CrossRef]
10. Murataliyev, M.; Degano, M.; Galea, M. A Novel Sizing Approach for Synchronous Reluctance Machines. *IEEE Trans. Ind. Electron.* **2021**, *68*, 2083–2095. [CrossRef]
11. Cavagnino, A.; Pellegrino, G.; Vaschetto, S.; Agamloh, E.B. Contribution to Offline Measurements of PMSM and SyRM Inductances. *IEEE Trans. Ind. Appl.* **2019**, *55*, 407–416. [CrossRef]
12. Pellegrino, G.; Boazzo, B.; Jahns, T.M. Magnetic Model Self-Identification for PM Synchronous Machine Drives. *IEEE Trans. Ind. Appl.* **2015**, *51*, 2246–2254. [CrossRef]
13. Hall, S.; Márquez-Fernández, F.J.; Alaküla, M. Dynamic Magnetic Model Identification of Permanent Magnet Synchronous Machines. *IEEE Trans. Energy Convers.* **2017**, *32*, 1367–1375. [CrossRef]
14. Wiedemann, S.; Hall, S.; Kennel, R.M.; Alaküla, M. Dynamic Testing Characterization of a Synchronous Reluctance Machine. *IEEE Trans. Ind. Appl.* **2018**, *54*, 1370–1378. [CrossRef]
15. Stumberger, B.; Stumberger, G.; Dolinar, D.; Hamler, A.; Trlep, M. Evaluation of saturation and cross-magnetization effects in interior permanent-magnet synchronous motor. *IEEE Trans. Ind. Appl.* **2003**, *39*, 1264–1271. [CrossRef]
16. Pescetto, P. Sensorless Commissioning and Control of High Anisotropy Synchronous Motor Drives. Ph.D. Dissertation, Politecnico di Torino, Turin, Italy, 2019.
17. Bedetti, N.; Calligaro, S.; Petrella, R. Stand-Still Self-Identification of Flux Characteristics for Synchronous Reluctance Machines Using Novel Saturation Approximating Function and Multiple Linear Regression. *IEEE Trans. Ind. Appl.* **2016**, *52*, 3083–3092. [CrossRef]
18. Hinkkanen, M.; Pescetto, P.; Mölsä, E.; Saarakkala, S.E.; Pellegrino, G.; Bojoi, R. Sensorless Self-Commissioning of Synchronous Reluctance Motors at Standstill Without Rotor Locking. *IEEE Trans. Ind. Appl.* **2017**, *53*, 2120–2129. [CrossRef]
19. Pescetto, P.; Pellegrino, G. Automatic Tuning for Sensorless Commissioning of Synchronous Reluctance Machines Augmented With High-Frequency Voltage Injection. *IEEE Trans. Ind. Appl.* **2018**, *54*, 4485–4493. [CrossRef]
20. Varvolik, V.; Prystupa, D.; Buticchi, G.; Peresada, S.; Galea, M.; Bozhko, S. Inverter Nonlinearity Effects on Self-Commissioning of Synchronous Reluctance Drives. In Proceedings of the 2021 24th International Conference on Electrical Machines and Systems (ICEMS), Gyeongju, Korea, 31 October–3 November 2021; pp. 1792–1797. [CrossRef]
21. Mingardi, D.; Morandin, M.; Bolognani, S.; Bianchi, N. On the Proprieties of the Differential Cross-Saturation Inductance in Synchronous Machines. *IEEE Trans. Ind. Appl.* **2017**, *53*, 991–1000. [CrossRef]
22. Saur, M.; Gaona Erazo, D.E.; Zdravkovic, J.; Lehner, B.; Gerling, D.; Lorenz, R.D. Minimizing Torque Ripple of Highly Saturated Salient Pole Synchronous Machines by Applying DB-DTFC. *IEEE Trans. Ind. Appl.* **2017**, *53*, 3643–3651. [CrossRef]
23. Varvolik, V.; Prystupa, D.; Buticchi, G.; Peresada, S.; Galea, M.; Bozhko, S. Co-Simulation Analysis for Performance Prediction of Synchronous Reluctance Drives. *Electronics* **2021**, *10*, 2154. [CrossRef]
24. Riccio, J.; Karamanakos, P.; Odhano, S.; Tang, M.; Nardo, M.D.; Zanchetta, P. A Direct Model Predictive Control Strategy for High-Performance Synchronous Reluctance Motor Drives. In Proceedings of the 2021 IEEE Energy Conversion Congress and Exposition (ECCE), Vancouver, BC, Canada, 10–14 October 2021; pp. 4704–4710. [CrossRef]
25. Pyrhonen, J.; Hrabovcova, V.; Semken, R. *Electrical Machine Drives Control: An Introduction*; Wiley: Hoboken, NJ, USA, 2016.